Journal of
Nanoscience and Nanotechnology
Vol. 11, 8206–8213, 2011

Plasma Processing of Nanomaterials: Emerging Technologies for Sensing and Energy Applications

Alberto Gasparotto[1,*], Davide Barreca[2], Daniela Bekermann[1], Anjana Devi[3], Roland A. Fischer[3], Chiara Maccato[1], and Eugenio Tondello[1]

[1] Department of Chemistry, Padova University and INSTM, 35131 Padova, Italy
[2] CNR-ISTM and INSTM, Department of Chemistry, Padova University, 35131 Padova, Italy
[3] Lehrstuhl für Anorganische Chemie II, Ruhr-University Bochum, 44780 Bochum, Germany

Plasma processing represents an attractive and versatile option for the fabrication of low-dimensional nanomaterials, whose chemical and physical properties can be conveniently tailored for the development of advanced technologies. In particular, Plasma Enhanced-Chemical Vapor Deposition (PE-CVD) is an appealing route to multi-functional oxide nanoarchitectures under relatively mild conditions, owing to the unique features and activation mechanisms of non-equilibrium plasmas. In this context, the potential of plasma-assisted fabrication in advanced nanosystem development is discussed. After a brief introduction on the basic categories of plasma approaches, the perspectives of application to CVD processes are commented, reporting on the growth and characterization of Co_3O_4 nanomaterials as a case study. Besides examining the interrelations between the material properties and the synthesis conditions, special focus is given to their emerging applications as catalysts for photo-assisted hydrogen production and solid state gas sensors.

Keywords: Plasma Processing, PE-CVD, Co_3O_4 Nanomaterials, Hydrogen Photo-Production, Gas Sensing.

RESEARCH ARTICLE

1. INTRODUCTION

The rapid and on-going progresses in the field of multi-functional nanomaterials has stimulated an increasing search for innovative fabrication techniques enabling to meet the challenges associated to specific requirements (from compositional uniformity to well-defined structural characteristics, such as aspect ratio, crystallographic orientation, size distribution, surface area...).[1–3] The control and modification of such features is essential in order to exploit the nanosystem properties that underpin advanced applications, from optoelectronics to photovoltaics, from self-cleaning to energy conversion and storage, catalysis and sensing.[4,5]

In the current tide of nanostructure preparation, plasma technology holds an outstanding promise for the manufacturing of a wide variety of materials, from powders to thin films, multi-layers, composites, nanotubes, nanowires.[4] Despite plasma-assisted approaches have long been used in the top-down scheme of micro-device fabrication, their application to the bottom-up synthesis of inorganic nanostructures with tailored features still represents a rather unexplored field.[2,5] What makes plasmas very attractive is their flexibility not only for the growth of nanosystems, but also for modifying their surface properties. Beside high-energy thermal plasmas, whose interaction with solid, liquid or gaseous precursors ensures fast production rates and a high crystallinity of the resulting material,[6,7] a considerable attention is actually focused on weakly ionized non-equilibrium plasmas, characterized by a much higher temperature for electrons than for ions ($\approx 10^4$ K in the former case).[2] The different mobility of such species induces the building up of an electric field (the sheath field) perpendicular to the solid surface at the plasma-solid interface.[8] This phenomenon accelerates cations towards the forming system, with its consequent bombardment and the development of peculiar growth directions and structural orientations.[5,9–11] In the case of porous/rough substrates, ion bombardment and the associated local energy transfer result in a typical infiltration power, enabling deposition to occur not only at the surface, but even in the inner system regions.[12] Such effects, in synergy with the excitation, ionization and dissociation of gas molecules promoted by "hot" electrons, activate a unique gas-phase and surface chemistry, diversifying material

*Author to whom correspondence should be addressed.

 1533-4880/2011/11/8206/008 doi:10.1166/jnn.2011.5023

features from those obtained by conventional gas-based synthetic routes.[4,13,14] A distinctive property of cold plasmas is their high chemical reactivity even in the absence of external thermal supplies, a key feature for the processing of heat-sensitive materials at temperatures close to the room one.[1,3,5] In addition, the temperature-dependent competition between growth and ablation phenomena may result in unique and often unexpected nano-organization.[15]

Among plasma-assisted methods, three main approaches are especially promising for the mild processing of nanomaterials (Fig. 1):[2]
(1) Plasma Enhanced-Chemical Vapor Deposition (PE-CVD), where gaseous molecular precursors are introduced into the plasma, whose role is either to activate the sole precursor, or to avoid/enhance peculiar growth effects on the substrate surface. The eventual use of metal catalyst nanoparticles may also be effective to this aim;[5,16]
(2) Sputtering, involving the plasma bombardment of an externally biased target and the consequent ejection of neutral and charged species, enabling a high versatility in the preparation of supported nanoparticles or nanocomposites;[12,17]
(3) Plasma treatment of solid materials, based on the exploitation of bombardment and etching effects to modify the system surface, producing the target nanostructures. As recently stated,[2] "there is some unresolved magic in this mechanism" and the underlying elementary processes have been the subject of detailed investigations.[5]

In general, deposition, ablation and surface modification processes are always concurrent and the predominance of one over the others can be attained by a judicious choice of the experimental parameters, including pressure, power density, flow rates and plasma composition.[2,13,14]

In this contribution, attention will be specifically devoted to the potential of PE-CVD routes in the preparation of metal oxide nanostructures with tailored features. As a selected and representative case study, we have chosen nanosystems based on cobalt (II, III) oxide (Co_3O_4), a *p*-type semiconductor that appears intriguing for a plethora of utilizations, including electrochromic devices, (photo)catalysts and gas sensors.[18–24] In this work, the relationships between the properties of supported Co_3O_4 nanomaterials and the experimental PE-CVD parameters will be presented and critically discussed as a function of the adopted molecular precursors. Special emphasis will be given to the quality of the obtained systems in terms of chemical composition, structure and morphology, whose control is indeed a crucial step for obtaining unique functional properties. In particular, preliminary representative examples will be provided on the photo-assisted production of H_2, one of the most significant energy vectors of the future,[25] from photo-reforming of ethanol/water solutions, and in the detection of gaseous H_2 and O_3, two flammable/toxic analytes whose reliable monitoring is of great practical importance.[11,24,26,27] To the best of our knowledge, only one report on photo-induced H_2 generation from supported Co_3O_4 systems is available in the literature to date,[28] whereas their application in hydrogen/ozone detection has been scarcely investigated.[24,29]

2. EXPERIMENTAL DETAILS

Supported Co_3O_4 nanodeposits were obtained by means of a previously described PE-CVD Radio-Frequency (RF, $\nu = 13.56$ MHz) apparatus.[15] Si(100) wafers and polycrystalline Al_2O_3 slides (thickness = 254 μm) were used as substrates after a suitable cleaning procedure.[9,26] Depositions were performed starting from

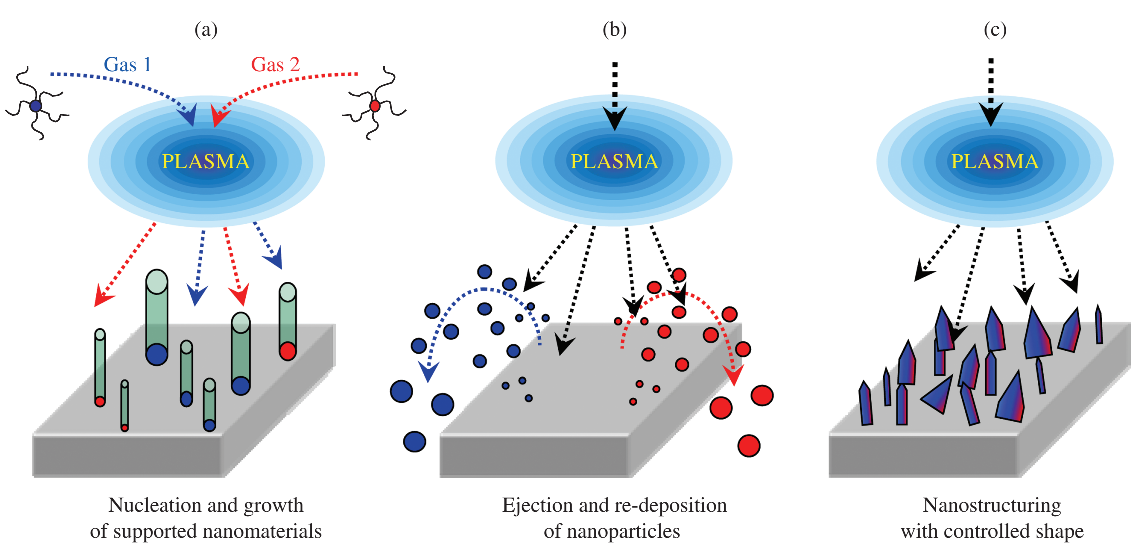

Fig. 1. Sketch of three different plasma-assisted routes to nanomaterials: (a) PE-CVD; (b) Sputtering; (c) Surface modification.

both first- and second-generation[30, 31] cobalt(II) precursors, namely [Co(dpm)$_2$] (dpm = 2,2,6,6-tetramethyl-3,5-heptanedionate) and [Co(hfa)$_2$•TMEDA] (hfa = 1,1,1,5,5,5-hexafluoro-2,4-pentanedionate; TMEDA = N,N,N',N'-tetramethylethylenediamine). These compounds, synthesized following previous literature procedures,[22, 32] were vaporized at 90 and 60 °C, respectively, and transported into the PE-CVD chamber by means of an Ar flow (purity = 5.0; rate = 60 sccm). Additional Ar (15 sccm) and O_2 (purity = 6.0; 20 sccm) flows were introduced into the reactor by independent inlets. In each experiment, lines for gas transport were heated at temperatures 30 °C higher than the vaporization ones, in order to prevent detrimental condensation phenomena. Depositions (duration = 1 h) were performed at a fixed pressure, RF-power and inter-electrodic distance of 1.0 mbar, 20 W and 6.0 cm, respectively. The growth temperature was varied in the 100–400 °C range.

X-ray Photoelectron Spectroscopy (XPS) measurements were run on a Perkin-Elmer Φ 5600ci spectrometer using a standard AlKα source (1486.6 eV), at a working pressure lower than 10^{-8} mbar. The reported Binding Energies (BEs, standard deviation = ±0.2 eV) were corrected for charging effects by assigning to the adventitious C1s line a BE of 284.8 eV.[33] The analysis involved Shirley-type background subtraction and, whenever necessary, spectral deconvolution, carried out by nonlinear least-squares curve fitting adopting Gaussian-Lorentzian sum functions. The atomic composition was calculated by peak integration, using sensitivity factors provided by Φ V5.4A software. Ar^+ sputtering was carried out at 4×10^{-8} mbar and 4.5 kV, with a raster size of 2×2 mm^2.

Glancing Incidence X-ray Diffraction (GIXRD) patterns were collected by a Bruker D8 Advance diffractometer (CuKα radiation, 40 kV, 40 mA), equipped with a Göbel mirror, at a fixed incidence angle of 3.0°. The average crystallite dimensions were estimated from line broadening by means of the Scherrer equation.

Field Emission-Scanning Electron Microscopy (FE-SEM) analyses were performed by a Zeiss SUPRA 40VP instrument. Plane-view and cross-sectional micrographs were acquired at primary beam acceleration voltages between 5 and 10 kV.

Photo-assisted H_2 production was carried out under UV irradiation (low-pressure mercury lamp, 125 W) by immersing Si(100)-supported systems (size = 1.5×2.0 cm^2) in CH_3CH_2OH/H_2O (1:1) solutions. Blank tests were performed on the bare Si(100) substrates, and no activity was observed either in the dark or upon illumination. A controlled flow of O_2 (2.5%) in Ar (flow rate = 15 ml $\times$ min^{-1}) was bubbled through the solution to transport the evolved gases to an Agilent HP 6890 Gas Cromatographer (GC), for an on-line product analysis.[34]

Gas sensing tests were performed at atmospheric pressure in a thermostatic sealed chamber with controlled temperature (20 °C) and relative humidity (40%). The experimental set-up and geometry of the contacts have already been reported.[35, 36] The analyses were carried out by the flow-through technique, using a constant flow rate of dry air (0.3 slm) and monitoring the sensor current as a function of the gas concentrations under a constant bias voltage (volt-amperometric technique). The sensor response and recovery times were determined as previously described.[37, 38]

3. RESULTS AND DISCUSSION

To exemplify the potential of PE-CVD in the fabrication of multi-functional oxide nanosystems, the following discussion will be focused on the synthesis and characterization of Co_3O_4-based materials. The system chemical composition was initially investigated by XPS. As evidenced by Figure 2, wide-scan spectra clearly displayed Co and O photopeaks, together with a weak C and F contribution (the latter for the sole trace **(b)**), whose origin is explained below. Irrespective of the adopted processing conditions, the Co2p peak position (BE(Co2p$_{3/2}$) = 780.2 eV) and shape agreed to a good extent with the presence of Co_3O_4 as the sole cobalt-containing phase.[23, 28, 32, 33, 39] This observation was further confirmed by the Auger α parameter, whose value was 1553.5 eV, a finger-print for pure Co_3O_4.[22, 36] The surface O/Co ratio of ≈1.5 was slightly

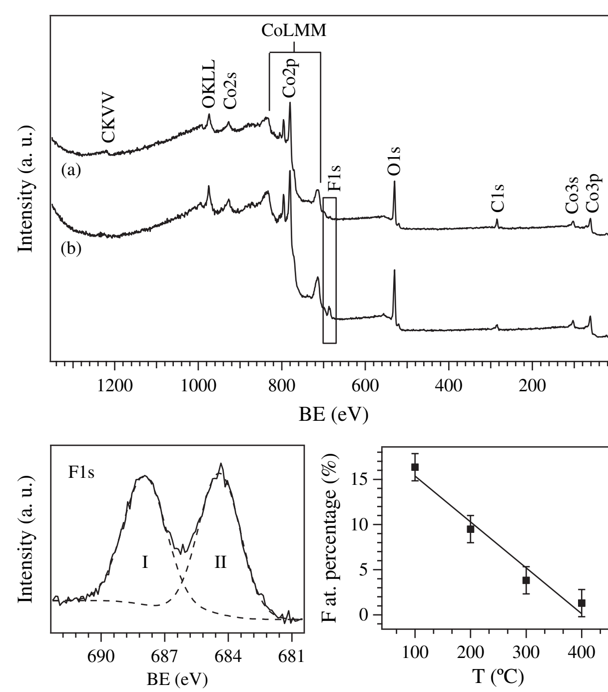

Fig. 2. Top: Surface XPS wide-scan spectrum for two PE-CVD cobalt oxide systems grown at 200 °C from: (a) [Co(dpm)$_2$]; (b) [Co(hfa)$_2$•TMEDA]. Bottom: Deconvolution of surface F1s peak for a Co_3O_4-based nanodeposit obtained at 100 °C and dependence of surface F content on the deposition temperature for Si(100)-supported samples obtained from [Co(hfa)$_2$•TMEDA].

higher than the expected stoichiometric value, and justified by the presence of surface hydroxyl/carbonate species arising from air exposure.[23,39,40] The main difference upon using [Co(dpm)$_2$] or [Co(hfa)$_2$•TMEDA] as starting sources was the presence of the F1s signal in the latter case (Fig. 2, upper panel, trace (**b**)). Such photopeak had the maximum intensity at a growth temperature of 100 °C (Fig. 2, lower panel) and could be fitted by means of two different components, located at 688.0(I) and 684.5(II) eV, respectively. Whereas the former could be ascribed to undecomposed precursor residuals, signal(II) was consistent with the presence of lattice fluorine incorporated in the Co_3O_4 network.[40,41] Upon increasing the deposition temperature from 100 to 400 °C, F content was progressively reduced from ≈16 to ≈1 at.% and, correspondingly, component(I) disappeared, suggesting thus an improved precursor decomposition at higher temperatures. Furthermore, in-depth analyses (not shown) indicated an almost constant fluorine concentration from the surface to the inner specimen regions, and, concomitantly, a vanishing of component(I) after 5 min of Ar^+ erosion. Such observations indicate that the presence of undecomposed precursor fragments at low temperatures was limited to the system surface. The above results indicate the potential of plasma processing for the controlled fluorine doping of Co_3O_4 materials, that has never been reported up to date. To this aim, it is worthwhile observing that the use of [Co(hfa)$_2$•TMEDA] in thermal CVD experiments always led to fluorine-free cobalt oxide nanosystems.[23,32,36]

Figure 3 displays GIXRD patterns for selected systems deposited both on Si(100) and Al_2O_3. As a general trend, all the spectra were in agreement with the formation of the spinel-type cubic Co_3O_4 phase,[42] but the relative intensity of the observed reflections was directly influenced by the growth temperature and the adopted precusor. Regarding the specimens obtained on Si(100) from [Co(dpm)$_2$], at 100 °C (trace i) only the signal of the (311) planes at $2\vartheta = 36.9°$ was present, which is the most intense even in the powder reference pattern. It is worth highlighting that the obtainment of crystalline deposits under such mild conditions is a peculiar effect of plasma activation, since in conventional thermal CVD analogous results were obtained for deposition temperatures not lower than 350 °C.[22,23] This goal is extremely attractive in view of possible technological applications involving depositions on thermally labile substrates, such as plastics and conductive polymers. At 400 °C, well-developed diffraction peaks could be clearly observed (trace ii). Furthermore, the intensity ratio between the (111) reflection (centered at $2\vartheta = 19.0°$) and the above mentioned (311) one was higher than that of the powder spectrum,[42] suggesting the possible occurrence of anisotropy/texturing effects. A qualitatively similar situation in terms of relative diffracted intensities was present for the deposit obtained at 100 °C from [Co(hfa)$_2$•TMEDA] (trace iii), whereas at 400 °C the

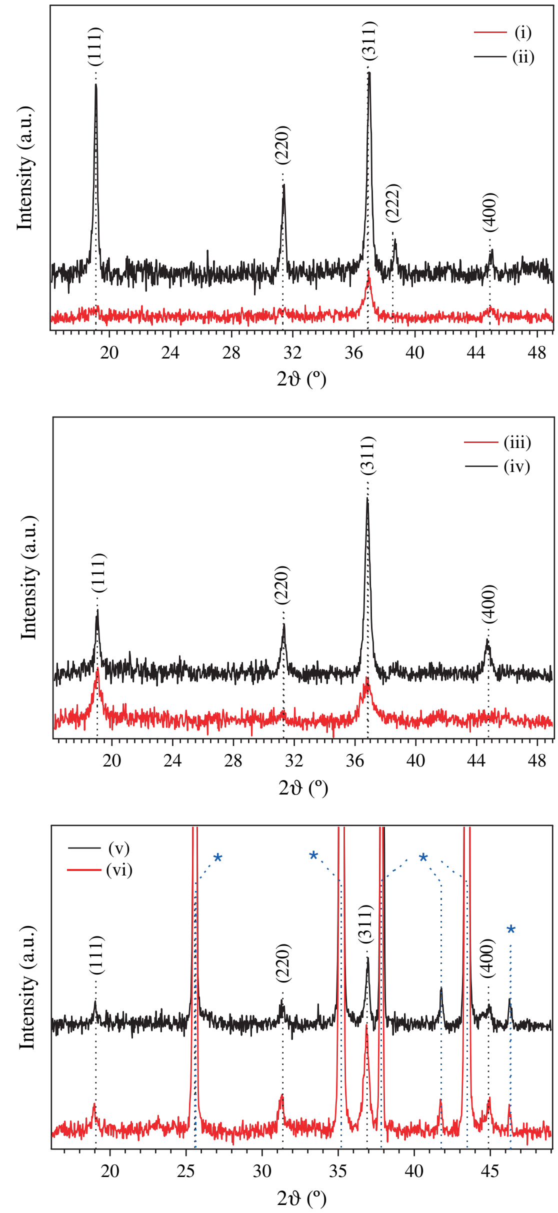

Fig. 3. GIXRD patterns for PE-CVD cobalt oxide nanosystems obtained: from [Co(dpm)$_2$] on Si(100), at 100 (i) and 400 °C (ii); from [Co(hfa)$_2$•TMEDA] on Si(100), at 100 (iii) and 400 °C (iv); on Al_2O_3 at 400 °C, from [Co(dpm)$_2$] (v) and [Co(hfa)$_2$•TMEDA] (vi). In the last case, stars (*) mark reflections attributed to the Al_2O_3 substrate.

pattern was in line with that expected for polycrystalline Co_3O_4 (trace iv). Overall, these features indicate that the precursor nature and decomposition pattern directly influenced the deposit structural characteristics.

In a different way, Al_2O_3-supported systems (Fig. 3, (v) and (vi)) always presented the same relative intensity ratios of the reference Co_3O_4 pattern. This phenomenon could be traced back to the polycrystalline nature and high roughness of this substrate, resulting in an isotropic growth of the deposited specimens.

Whereas for samples grown on alumina the typical mean crystallite size was ≈30 nm, in the case of Si(100)-supported specimens the average nanocrystal dimensions underwent an increase from ≈10 nm, at 100 °C, to ≈30 nm, at 200–400 °C, irrespective of the used precursor. The initial size increase with deposition temperature (from 100 to 200 °C) can be ascribed to a higher supply of thermal energy to the depositing system, progressively favoring the nanocrystal growth. On the other hand, the dimension constancy above 200 °C could be related to the competition between deposition and ablation processes characterizing the used plasmas, which plays a key role in the obtainment of materials with a controlled nanostructured organization.[15]

Important information on the interrelations between the system morphology and the synthesis parameters was gained by FE-SEM analyses (Fig. 4). As a general rule, the use of [Co(hfa)$_2$•TMEDA] enabled the obtainment of a higher nanodeposit thickness with respect to [Co(dpm)$_2$]. This feature was ascribed to a higher mass supply of the former precursor to the growth surface under the adopted experimental conditions.[22,32] At 100 °C (Fig. 4, (i) and (iii)), Si(100)-supported samples were formed by small interconnected globular particles, resulting in rather compact deposits. At higher deposition temperatures, an enhanced particle size and a more pronounced faceting became evident. In particular, at 400 °C the system obtained from [Co(dpm)$_2$] (Fig. 4, (ii)) was dominated by well-defined pyramidal aggregates, likely due to the preferential exposure of low surface energy {111} crystallographic planes,[23] in line with GIXRD results (Fig. 3, (ii)). For the sample deposited at 400 °C from [Co(hfa)$_2$•TMEDA] (Fig. 4, (iv)), such a faceting was less evident, consistently with the absence of any appreciable texturing effect (compare Fig. 3, (iv)). As concerns Si(100)-supported specimens, a progressive increase of the mean aggregate size from ≈10 to ≈30 nm took place upon increasing the deposition temperature from 100 to 400 °C. A comparison of such values with the ones evaluated by the Scherrer equation suggested that the majority of particles observed in Figure 4 were single-domain crystallites.

In a different way, for alumina-supported samples (Fig. 4, (v) and (vi)) FE-SEM micrographs were dominated by the presence of globular Al_2O_3 particles with a mean size of ≈600 nm, uniformly covered by low-sized Co_3O_4 nanoaggregates. This unique morphology, arising from the typical conformal coverage of CVD-related techniques, is likely associated with a high active area, an attractive feature in view of gas sensing applications.[38]

Subsequently, the attention was focused on the analysis of the system functional properties in photo-assisted hydrogen generation and in the detection of gaseous analytes, two applicative practical fields where Co_3O_4-based nanosystems have only seldom been utilized,[28,36] and the potential of plasma processing has never been exploited.

Hydrogen production experiments were performed in CH_3CH_2OH/H_2O solutions for a twofold reason. First,

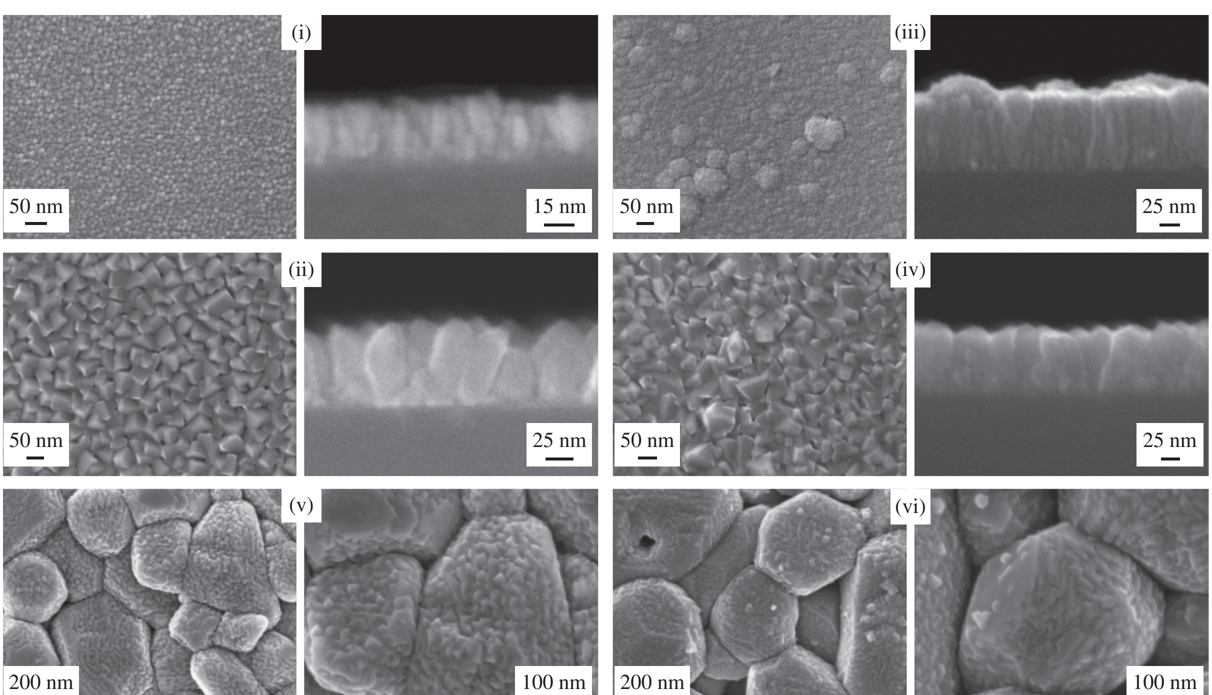

Fig. 4. Representative FE-SEM cross-sectional and plane-view micrographs of Co_3O_4-based nanodeposits obtained: from [Co(dpm)$_2$] on Si(100), at 100 (i) and 400 °C (ii); from [Co(hfa)$_2$•TMEDA] on Si(100), at 100 (iii) and 400 °C (iv); on Al_2O_3 at 400 °C, from [Co(dpm)$_2$] (v) and [Co(hfa)$_2$•TMEDA] (vi).

RESEARCH ARTICLE

ethanol can directly take part to H_2 generation through photo-reforming processes, leading to the concomitant evolution of carbon-containing byproduts, like CH_3CHO, CO, and CO_2. In addition, alcohols typically act as scavengers of photo-generated holes, preventing their detrimental recombination with the produced electrons and increasing thus their availability in the photocatalytic process.[34] To avoid an undesired $Co_3O_4 \rightarrow CoO$ reduction in the presence of the photo-produced hydrogen and catalyst poisoning by carbon-containing residuals, photocatalytic tests have been carried out in the presence of oxygen.[28]

As an example, Figure 5 reports the hydrogen production rate as a function of UV irradiation time for a selected Co_3O_4 specimen. After an initial induction period of $\approx$1 h, a significant H_2 evolution (up to $\approx$8 μmol $\times$ $h^{-1} \times cm^{-2}$), that remained almost constant for the following 2 h of illumination, was observed. Subsequently, a modest, though progressive, rate decrease took place. A similar phenomenon, that was observed for all the tested Co_3O_4 nanodeposits, could be attributed to the occurrence of photoleaching phenomena, with a consequent catalyst degradation upon prolonged utilization. Hence, the optimization of the system performances requires the obtainment of a compromise between their reactivity and time stability. Nonetheless, it is worth highlighting that, after photocatalytic tests, the samples did not show any evidence of mechanical detachment from Si(100) substrates, a result of great importance in view of their eventual practical utilization.

Finally, the capability of the obtained systems to act as solid state gas sensors was tested in the detection of both H_2 and O_3, two colourless, extremely reactive and dangerous gases. Preliminary results are shown in Figure 6, that reports the dynamical responses to square concentration pulses of both analytes for two selected Co_3O_4 sensors supported on Al_2O_3. In the case of hydrogen, a reducing gas (Fig. 6(a)), the current flowing through the sample decreased upon contact with the analyte, whereas an opposite trend was observed upon exposure to ozone, a strong oxidizing gas (Fig. 6(b)). Such a behavior is typical for

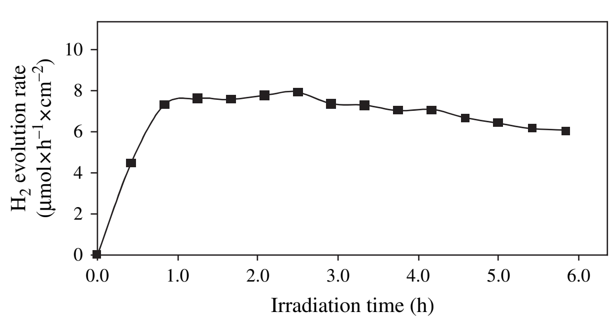

Fig. 5. Dependence of hydrogen evolution rate on irradiation time for a cobalt oxide specimen deposited from [$Co(hfa)_2$•TMEDA] on Si(100) at 300 °C.

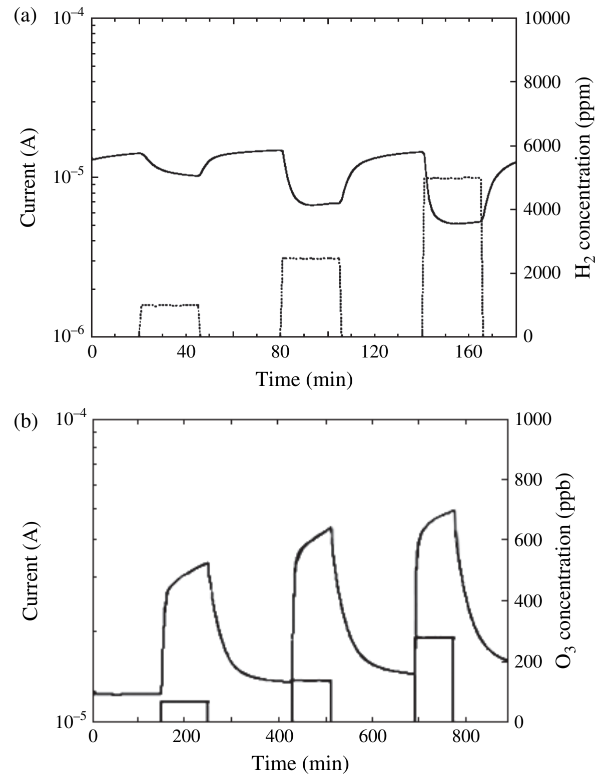

Fig. 6. Representative kinetic responses produced by steps in hydrogen and ozone concentrations for Co_3O_4-based sensors synthesized on Al_2O_3: (a) from [$Co(hfa)_2$•TMEDA], at 400 °C; (b) from [$Co(dpm)_2$], at 200 °C. In both cases, the working temperature was 200 °C.

sensors based on *p*-type semiconductors, like Co_3O_4.[39] In fact, the interaction of reducing gases with chemisorbed oxygen species produces an electron release, with a consequent decrease of the majority *p*-type carriers and a parallel drop-off of the measured current.[36,37] Conversely, the sensor interaction with oxidizing analytes, like ozone, produces an electron withdrawal from the system and a concomitant current amplification.[21,27,29] A deeper observation of Figure 6(b) indicated that, in the presence of O_3, the experimental curve increased rapidly and subsequently more slowly up to the end of the pulse. Such a phenomenon, already observed in ozone sensing,[29] indicated that the chemisorption of this analyte on Co_3O_4 surface was the bottleneck in determining the resulting current variation.[26]

From the curves plotted in Figure 6, typical response times of 5 and 20 min could be estimated in the detection of hydrogen and ozone, respectively, whereas the corresponding recovery times were 10 and 45 min. Despite these values were not exceptionally low, in the case of hydrogen they compared favorably with those recently reported for Co_3O_4 nanodeposits obtained by thermal CVD from [$Co(hfa)_2$•TMEDA].[36] As a general rule, it is worthwhile noticing that the registered current variations were proportional to the injected target gas concentrations, pointing out to reversible interactions between the

RESEARCH ARTICLE

sensing element and the analytes and enabling thus to rule out any significant saturation effect. The improved reversibility even at lower operating temperatures with respect to Co_3O_4 sensors obtained by thermal CVD[36] can be traced back to the tailored system morphology and the reduced aggregate size, that are likely to be responsible for enhanced current modulation upon interaction with the target analytes.[35] This finding is of great importance in view of quantitative determination of highly flammable/toxic species, like hydrogen and ozone.

4. CONCLUSIONS AND OUTLOOK

In this manuscript we have attempted to describe the key distinctive features of plasma-assisted approaches, that candidate themselves as highly controllable strategies for the fabrication of supported functional nanomaterials. The peculiar homogeneous and hetereogeneous activation mechanisms occurring in the used plasmas can enable the selective manipulation of different nanosized building blocks, thus leading to a fine tailoring of the target product features. To this aim, the reader can find relevant examples in the cited literature, especially regarding the integration of plasma techniques with other nanofabrication approaches.

The convincing evidence for the fruitfulness of the above routes is demonstrated in the case of PE-CVD of Co_3O_4-based nanomaterials, obtained from first- and second-generation β-diketonate Co(II) complexes. It has been shown that plasma processing enables a wide tuning of the system composition and morphology, with associated structural characteristics variable as a function of the deposition temperature and precursor nature. Most importantly, many of these features are unattainable without plasma assistance. Preliminary data open up intriguing perspectives on the possible engineering of the present Co_3O_4-based nanosystems as multi-functional platforms for both energy and sensing applications.

Nevertheless, the knowledge presented in this article still lacks the understanding of many important phenomena, and leaves open questions on both fundamental and applicative sides. First, a thorough comprehension of the nucleation and growth stages leading to a peculiar nano-organization will provide an important basis in view of eventual scale-up of the described approaches. Continued work along these lines will be devoted to a deeper insight into the relationships between the system functional properties and plasma conditions, in an attempt to achieve superior performances in terms of both time stability and efficiency. In this regard, particular efforts will also be devoted to investigate the effect of fluorine doping on both the Co_3O_4 functional applications reported in this paper.

Acknowledgments: This work was supported by funding from the European Community's Seventh Framework Programme (FP7/2007–2013; grant agreement *n*° ENHANCE-238409). PRIN-COFIN 2008, Padova University PRAT 2008/2010, and Regione Lombardia-INSTM PICASSO program are also acknowledged for financial support. Thanks are due to Professor P. Fornasiero, Dr. V. Gombac and Dr. T. Montini (Trieste University, Italy) for H_2 photo-production experiments, to Professor G. Sberveglieri and Dr. E. Comini (Brescia University, Italy) for gas sensing tests and to Dr. M. Gavagnin, Dr. G. Carraro and Mr. A. Ravazzolo (CNR-ISTM, Padova University, Italy) for synthetic and technical assistance.

References and Notes

1. M. Wolter, I. Levchenko, H. Karsten, S. Kumar, and K. Ostrikov, *J. Appl. Phys.* 108, 053302 (**2010**).
2. J. Zheng, R. Yang, L. Xie, J. Qu, Y. Liu, and X. Li, *Adv. Mater*. 22, 1451 (**2010**).
3. S. Mathur, T. Ruegamer, N. Donia, and H. Shen, *J. Nanosci. Nanotechnol.* 8, 2597 (**2008**).
4. K. Ostrikov, I. Levchenko, S. Xu, S. Y. Huang, Q. J. Cheng, J. D. Long, and M. Xu, *Thin Solid Films* 516, 6609 (**2008**).
5. K. Ostrikov, I. Levchenko, U. Cvelbar, M. Sunkara, and M. Mozetic, *Nanoscale* 2, 2012 (**2010**).
6. A. V. Samokhin, N. V. Alekseev, and Y. V. Tsvetkov, *High Energy Chem.* 40, 93 (**2006**).
7. T. Ishigaki and J. G. Li, *Sci. Technol. Adv. Mater*. 8, 617 (**2007**).
8. D. L. Smith, Thin Film Deposition: Principles and Practice, McGraw-Hill, USA (**1995**).
9. D. Bekermann, A. Gasparotto, D. Barreca, L. Bovo, A. Devi, R. A. Fischer, O. I. Lebedev, C. Maccato, E. Tondello, and G. Van Tendeloo, *Cryst. Growth Des*. 10, 2011 (**2010**).
10. D. Bekermann, A. Gasparotto, D. Barreca, A. Devi, R. A. Fischer, M. Kete, U. Lavrenčič Štangar, O. I. Lebedev, C. Maccato, E. Tondello, and G. Van Tendeloo, *ChemPhysChem* 11, 2337 (**2010**).
11. D. Barreca, D. Bekermann, E. Comini, A. Devi, R. A. Fischer, A. Gasparotto, C. Maccato, C. Sada, G. Sberveglieri, and E. Tondello, *CrystEngComm* 12, 3419 (**2010**).
12. L. Armelao, D. Barreca, G. Bottaro, A. Gasparotto, C. Maccato, E. Tondello, O. I. Lebedev, S. Turner, G. Van Tendeloo, C. Sada, and U. Lavrenčič Štangar, *ChemPhysChem* 10, 3249 (**2009**).
13. S. Xu, K. Ostrikov, J. D. Long, and S. Y. Huang, *Vacuum* 80, 621 (**2006**).
14. K. Ostrikov, J. D. Long, P. P. Rutkevych, and S. Xu, *Vacuum* 80, 1126 (**2006**).
15. D. Barreca, A. Gasparotto, E. Tondello, C. Sada, S. Polizzi, and A. Benedetti, *Chem. Vap. Deposition* 9, 199 (**2003**).
16. Y. Xia, P. Yang, Y. Sun, Y. Wu, B. Mayers, B. Gates, Y. Yin, F. Kim, and H. Yan, *Adv. Mater.* 15, 353 (**2003**).
17. D. Barreca, A. Gasparotto, C. Maccato, and E. Tondello, *Nanotechnology* 19, 255602 (**2008**).
18. W. Y. Li, L. N. Xu, and J. Chen, *Adv. Funct. Mater*. 15, 851 (**2005**).
19. X. Xie, Y. Li, Z.-Q. Liu, M. Haruta, and W. Shen, *Nature* 458, 746 (**2009**).
20. M. Casas-Cabanas, G. Binotto, D. Larcher, A. Lecup, V. Giordani, and J.-M. Tarascon, *Chem. Mater.* 21, 1939 (**2009**).
21. P. Konova, M. Stoyanova, A. Naydenov, St. Christoskova, and D. Mehandjiev, *Appl. Catal., A* 298, 109 (**2006**).
22. D. Barreca, C. Massignan, S. Daolio, M. Fabrizio, C. Piccirillo, L. Armelao, and E. Tondello, *Chem. Mater.* 13, 588 (**2001**).
23. D. Barreca, A. Gasparotto, O. I. Lebedev, C. Maccato, A. Pozza, E. Tondello, S. Turner, and G. Van Tendeloo, *CrystEngComm* 12, 2185 (**2010**).
24. P. A. Tikhonov, A. T. Nakusov, I. A. Drozdova, M. V. Kalinina, and A. I. Domanskii, *Glass Phys. Chem.* 31, 700 (**2005**).

RESEARCH ARTICLE

25. A. Demirbas, Biohydrogen: For Future Engine Fuel Demands, Springer-Verlag, London, UK (**2009**).
26. D. Barreca, D. Bekermann, E. Comini, A. Devi, R. A. Fischer, A. Gasparotto, C. Maccato, G. Sberveglieri, and E. Tondello, *Sens. Actuators, B* 149, 1 (**2010**).
27. C. Baratto, M. Ferroni, G. Faglia, and G. Sberveglieri, *Sens. Actuators, B* 118, 221 (**2006**).
28. D. Barreca, P. Fornasiero, A. Gasparotto, V. Gombac, C. Maccato, A. Pozza, and E. Tondello, *Chem. Vap. Deposition* 16, 296 (**2010**).
29. W. Belkacem, A. Labidi, J. Guérin, N. Mliki, and K. Aguir, *Sens. Actuators, B* 132, 196 (**2008**).
30. G. Malandrino and I. L. Fragalà, *Coord. Chem. Rev*. 250, 1605 (**2006**).
31. G. Malandrino, R. G. Toro, R. Lo Nigro, and I. L. Fragalà, *ECS Trans*. 25, 125 (**2009**).
32. G. Bandoli, D. Barreca, A. Gasparotto, C. Maccato, R. Seraglia, E. Tondello, A. Devi, R. A. Fischer, and M. Winter, *Inorg. Chem* 48, 82 (**2009**).
33. D. Briggs and M. P. Seah, Practical Surface Analysis, Chichester, Wiley, UK (**1983**).
34. D. Barreca, P. Fornasiero, A. Gasparotto, V. Gombac, C. Maccato, T. Montini, and E. Tondello, *ChemSusChem* 2, 230 (**2009**).
35. D. Barreca, A. Gasparotto, C. Maccato, C. Maragno, E. Tondello, E. Comini, and G. Sberveglieri, *Nanotechnology* 18, 125502 (**2007**).
36. D. Barreca, E. Comini, A. Gasparotto, C. Maccato, A. Pozza, C. Sada, G. Sberveglieri, and E. Tondello, *J. Nanosci. Nanotechnol.* 10, 8054 (**2010**).
37. D. Barreca, E. Comini, A. Gasparotto, C. Maccato, C. Sada, G. Sberveglieri, and E. Tondello, *Sens. Actuators, B* 141, 270 (**2009**).
38. D. Barreca, E. Comini, A. P. Ferrucci, A. Gasparotto, C. Maccato, C. Maragno, G. Sberveglieri, and E. Tondello, *Chem. Mater*. 19, 5642 (**2007**).
39. D. Patil, P. Patil, V. Subramanian, P. A. Joy, and H. S. Potdar, *Talanta* 81, 37 (**2010**).
40. J. F. Moulder, W. F. Stickle, P. W. Sobol, and K. D. Bomben, Handbook of X-ray Photoelectron Spectroscopy, Perkin-Elmer, Eden Prairie, MN (**1992**).
41. NIST X-ray Photoelectron Spectroscopy Database, version 3.5 (**2007**), http://srdata.nist.gov/xps
42. Pattern # 42-1467, JCPDS (**2000**).

Received: 12 April 2011. Accepted: 7 July 2011.